Disentangling the high- and low-cutoff scales via the trilinear Higgs couplings in the type-I two-Higgs-doublet model

Sin Kyu Kang,[1,*] Jinheung Kim,[2,†] Soojin Lee,[2,‡] and Jeonghyeon Song[2,§]
[1]*School of Natural Science, Seoul National University of Science and Technology, Seoul 139-743, Korea*
[2]*Department of Physics, Konkuk University, Seoul 05029, Republic of Korea*

(Received 10 October 2022; accepted 9 January 2023; published 26 January 2023)

The type-I two-Higgs-doublet model in the inverted Higgs scenario can retain the theoretical stability all the way up to the Planck scale. The Planck-scale cutoff $\Lambda_{\rm cut}^{\rm Planck}$ directly impacts the mass spectra such that all the extra Higgs boson masses should be light below about 160 GeV. However, the observation of the light masses of new Higgs bosons does not indicate the high-cutoff scale because a low-cutoff scale can also accommodate the light masses. Over the viable parameter points that satisfy the theoretical requirements and the experimental constraints, we show that the trilinear Higgs couplings for low $\Lambda_{\rm cut}$ are entirely different from those for the Planck-scale cutoff. The most sensitive coupling to the cutoff scale is from the h-h-h vertex, where h is the lighter CP-even Higgs boson at a mass below 125 GeV. The gluon fusion processes of $gg \to hh$ and $gg \to AA$ are insensitive to the cutoff scale, yielding a small variation of the production cross sections, $\mathcal{O}(1)$ fb, according to $\Lambda_{\rm cut}$. The smoking-gun signature is from the triple Higgs production of $q\bar{q}' \to W^* \to H^\pm hh$, which solely depends on the h-h-h vertex. The cross section for $\Lambda_{\rm cut} = 1$ TeV is about 10^3 times larger than that for the Planck-scale cutoff. Since the decay modes of $H^\pm \to W^* h/W^* A$ and $h/A \to bb$ are dominant, the process yields the $6b + \ell\nu$ final state, which enjoys an almost background-free environment. Consequently, the precision measurement of $pp \to H^\pm hh$ can probe the cutoff scale of the model.

DOI: 10.1103/PhysRevD.107.015025

I. INTRODUCTION

Up to today, all of the measurements of the production cross sections of the standard model (SM) particles at high-energy colliders are in good agreement with the SM predictions [1], including the observed Higgs boson with a mass of 125 GeV [2–16]. Nevertheless, our minds are rarely in satisfaction with the SM, because of the unsolved questions, such as the naturalness problem, baryogenesis, nonzero neutrino masses, fermion mass hierarchy, the origin of CP violation in the quark sector, and the identity of dark matter. We continue our journey in the quest for the ultimate theory.

A crucial question is whether the ultimate theory shall reveal its whole structure at one energy scale. The answer is much more likely to be *no* when looking back on the SM, the only reliable guideline at this moment. We witnessed the emergence of SM particles in stages. The same phenomena could happen in the ultimate theory. In other words, the final theory may consist of multilevel submodels. The first-stage new physics (NP) model[1] describes our Universe up to a particular energy scale $\Lambda_{\rm cut}$ and then hands over its role to the second-stage NP model. $\Lambda_{\rm cut}$ could be as high as the Planck scale or as low as 10 TeV. Then can an observable distinguish the high and low $\Lambda_{\rm cut}$? This is the driving question in our paper.

For the first-stage NP model, we consider the two-Higgs-doublet model (2HDM) since many fundamental questions are closely related to the Higgs sector. The 2HDM provides the answers to some questions. For example, the first-order electroweak phase transition in the 2HDM can explain the baryogenesis [17–21]. However, the model cannot address all the fundamental questions, which makes it a suitable candidate for the first-stage NP model.

Then the next question is how to calculate the energy scale at which the second-stage NP model appears. A good

---

[*] skkang@snut.ac.kr
[†] jinheung.kim1216@gmail.com
[‡] soojinlee957@gmail.com
[§] jhsong@konkuk.ac.kr

[1] Two different structures exist for the first-stage NP model. It can take over the SM from a high-energy scale, accommodating new heavy particles with the multi-TeV masses. Or it coexists with the SM at the electroweak scale so that the new particles have the intermediate masses.

way is to calculate the cutoff scale of the 2HDM. Even though the theoretical requirements (unitarity, perturbativity, and vacuum stability) are satisfied at the electroweak scale, they can be broken at a higher energy scale $\Lambda_{\rm cut}$ because the parameters evolve under renormalization group equations (RGEs) [22–28]. Since it implies the advent of the second-stage NP model, we call $\Lambda_{\rm cut}$ the cutoff scale of the model.

In the literature, the high-energy scale behavior of the 2HDM has been extensively studied. Most studies are focused on the impact of high $\Lambda_{\rm cut}$ on the extra Higgs boson masses [26,29–37]. However, observing the scalar mass spectrum that high $\Lambda_{\rm cut}$ predicts does not guarantee that $\Lambda_{\rm cut}$ is high. In this paper, we focus on the type I of the 2HDM in the inverted Higgs scenario where the heavier CP-even scalar H is the observed Higgs boson [38–40]. The model can accommodate the cutoff scale all the way up to the Planck scale [35]. As illustrated in Fig. 1, the allowed points of $(M_A, M_{H^\pm})$ for $\Lambda_{\rm cut} = 10^{18}$ GeV (red points) are overlapped with those for $\Lambda_{\rm cut} = 10$ TeV (gray points). Two points in cyan, one for $\Lambda_{\rm cut} = 10$ TeV and the other for $\Lambda_{\rm cut} = 10^{18}$ GeV, have the same M_A and $M_{H^\pm}$. We need an alternative observable to disentangle the high- and low-cutoff scales. The measurement of $\tan\beta$, the ratio of two vacuum expectation values of two-Higgs-doublet fields, is tricky in type I when $\tan\beta$ is large. In type I, all the Yukawa couplings of the beyond the SM (BSM) Higgs bosons are inversely proportional to $\tan\beta$ in the Higgs alignment limit. So, the main production channels of $gg \to A/h$ and $t \to H^\pm b$ are suppressed by large $\tan\beta$. In addition, the branching ratios of all the fermionic decay modes are insensitive to $\tan\beta$ in type I. We need alternative observables to probe the cutoff scale.

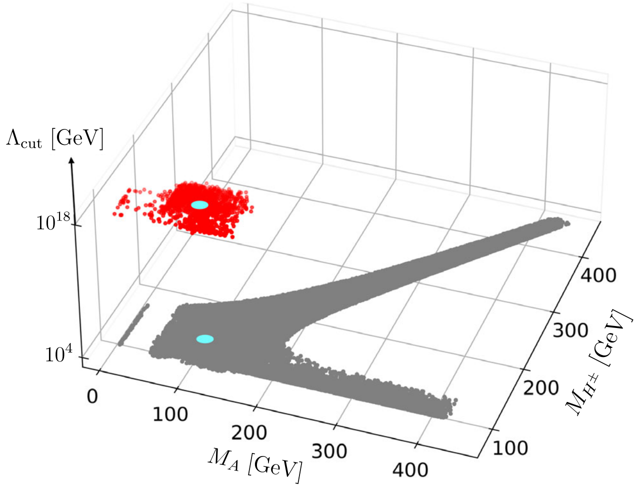

FIG. 1. Allowed $(M_A, M_{H^\pm})$ with the cutoff scales of $\Lambda_{\rm cut} = 10$ TeV (gray points) and $\Lambda_{\rm cut} = 10^{18}$ GeV (red points) in the inverted type I, over the viable parameter points that satisfy the theoretical requirements and the experimental constraints. Two points in cyan yield the same M_A and $M_{H^\pm}$.

We will show that the trilinear Higgs couplings can play the role. In particular, the value of the h-h-h vertex λ_{hhh} is highly sensitive to the cutoff scale. To probe the trilinear Higgs couplings at the LHC, we will study the di-Higgs processes of $gg \to hh$ and $gg \to AA$ and the tri-Higgs processes of $pp \to H^\pm hh$. The gluon fusion production of $gg \to h/H \to hh/AA$ is to be shown insensitive to $\Lambda_{\rm cut}$ because of the destructive interference between the h and H contributions. We will show that the tri-Higgs process $pp \to H^\pm hh$ is the best to measure the cutoff scale because the signal rate is solely dependent on λ_{hhh}, yielding $\sigma_{\Lambda_{\rm cut}=1\ {\rm TeV}}/\sigma_{\Lambda_{\rm cut}=10^{18}\ {\rm GeV}} \sim 10^3$. Considering the dominant decay modes of $H^\pm$ and h, we will suggest for the first time the $6b + \ell\nu$ final state as an efficient discriminator between the high- and low-cutoff scales. These are our new contributions.

The paper is organized in the following way. In Sec. II, we briefly review the type I in the inverted scenario. Section III describes the methods of the parameter scanning and the calculation of $\Lambda_{\rm cut}$. The characteristics of the viable parameter points with high $\Lambda_{\rm cut}$ are also presented. In Sec. IV, we calculate the correlation between the trilinear Higgs couplings and the cutoff scale. Section V deals with the LHC phenomenology. Based on the study of the branching ratios of the extra Higgs bosons, we will suggest efficient observables to distinguish the high- and low-cutoff scales. Finally, we conclude in Sec. VI.

II. REVIEW OF TYPE I OF 2HDM IN THE INVERTED SCENARIO

The 2HDM introduces two $SU(2)_L$ complex scalar doublet fields with hypercharge $Y = 1$, Φ_1 and Φ_2 [41],

$$\Phi_i = \begin{pmatrix} w_i^+ \\ \frac{v_i + \rho_i + i\eta_i}{\sqrt{2}} \end{pmatrix}, \qquad (i = 1, 2) \tag{1}$$

where v_1 and v_2 are the nonzero vacuum expectation values of Φ_1 and Φ_2, respectively. The ratio of v_2/v_1 defines the mixing angle β via $\tan\beta = v_2/v_1$. For notational simplicity, we use $s_x = \sin x$, $c_x = \cos x$, and $t_x = \tan x$ in what follows. The combination of v_1 and v_2, $v = \sqrt{v_1^2 + v_2^2} = 246$ GeV, spontaneously breaks the electroweak symmetry. To prevent flavor-changing neutral currents at tree level, we impose a discrete Z_2 symmetry under which $\Phi_1 \to \Phi_1$ and $\Phi_2 \to -\Phi_2$ [42,43]. We allow softly broken Z_2 symmetry since it does not affect the RGE of the dimensionless quartic couplings [44]: the hard Z_2 breaking in the Yukawa sector causes too fast growth of the scalar quartic couplings in the RG running [32].

For simplicity, we employ a CP-conserving scalar potential that softly breaks the Z_2 symmetry, which is given by

$$\begin{aligned} V_\Phi = {} & m_{11}^2 \Phi_1^\dagger \Phi_1 + m_{22}^2 \Phi_2^\dagger \Phi_2 - m_{12}^2 (\Phi_1^\dagger \Phi_2 + \text{H.c.}) \\ & + \frac{1}{2}\lambda_1 (\Phi_1^\dagger \Phi_1)^2 + \frac{1}{2}\lambda_2 (\Phi_2^\dagger \Phi_2)^2 + \lambda_3 (\Phi_1^\dagger \Phi_1)(\Phi_2^\dagger \Phi_2) \\ & + \lambda_4 (\Phi_1^\dagger \Phi_2)(\Phi_2^\dagger \Phi_1) + \frac{1}{2}\lambda_5 [(\Phi_1^\dagger \Phi_2)^2 + \text{H.c.}], \end{aligned} \qquad (2)$$

where the m_{12}^2 term softly breaks the Z_2 symmetry. The scalar potential V_Φ yields five physical Higgs bosons, the lighter CP-even scalar h, the heavier CP-even scalar H, the CP-odd pseudoscalar A, and a pair of charged Higgs bosons $H^\pm$. Relations of mass eigenstates with weak eigenstates in terms of two mixing angles of α and β are referred to Ref. [45]. The SM Higgs boson is a linear combination of h and H, given by

$$h_{\text{SM}} = s_{\beta-\alpha} h + c_{\beta-\alpha} H. \qquad (3)$$

The observed Higgs boson at a mass of 125 GeV at the LHC [2–16] has so far agreed with the predictions for the SM Higgs boson. The SM-like Higgs boson strongly motivates the Higgs alignment limit in the 2HDM. Two scenarios exist for the limit, the normal scenario where $h_{\text{SM}} = h$ (i.e., $s_{\beta-\alpha} = 1$) and the inverted scenario where $h_{\text{SM}} = H$ (i.e., $c_{\beta-\alpha} = 1$). In this paper, we concentrate on the inverted scenario in the Higgs alignment limit,

$$M_H = 125~\text{GeV}, \qquad c_{\beta-\alpha} = 1. \qquad (4)$$

Then we have the following five parameters:

$$\{m_h, M_A, M_{H^\pm}, t_\beta, m_{12}^2\}, \qquad (5)$$

which define one parameter point. Then, the quartic coupling constants in V_Φ are written as [46]

$$\begin{aligned} \lambda_1 &= \frac{1}{v^2}[m_{125}^2 + t_\beta^2 (m_h^2 - M^2)], \\ \lambda_2 &= \frac{1}{v^2}\left[m_{125}^2 + \frac{1}{t_\beta^2}(m_h^2 - M^2)\right], \\ \lambda_3 &= \frac{1}{v^2}[m_{125}^2 - m_h^2 - M^2 + 2M_{H^\pm}^2], \\ \lambda_4 &= \frac{1}{v^2}[M^2 + M_A^2 - 2M_{H^\pm}^2], \\ \lambda_5 &= \frac{1}{v^2}[M^2 - M_A^2], \end{aligned} \qquad (6)$$

where $m_{125} = 125$ GeV and $M^2 = m_{12}^2/(s_\beta c_\beta)$.

The Yukawa couplings to the SM fermions are parametrized as

$$\begin{aligned} \mathcal{L}^{\text{Yuk}} = {} & -\sum_f \left(\frac{m_f}{v} \xi_f^h \bar{f} f h + \frac{m_f}{v} \kappa_f^H \bar{f} f H - i \frac{m_f}{v} \xi_f^A \bar{f} \gamma_5 f A \right) \\ & - \left\{ \frac{\sqrt{2}}{v} \bar{t} (m_t \xi_t^A \mathrm{P}_- + m_b \xi_b^A \mathrm{P}_+) b H^+ \right. \\ & \left. + \frac{\sqrt{2} m_\tau}{v} \xi_\tau^A \bar{\nu}_\tau P_+ \tau H^+ + \text{H.c.} \right\}, \end{aligned} \qquad (7)$$

which are different according to the 2HDM type. In this work, we focus on type I. To facilitate the discussion below, we will call the type I with the conditions of Eq. (4) the inverted type I. Then the Higgs coupling modifiers are

$$\xi_f^H = 1, \qquad \xi_{t,b,\tau}^h = \frac{1}{t_\beta}, \qquad \xi_t^A = -\xi_{b,\tau}^A = \frac{1}{t_\beta}. \qquad (8)$$

The trilinear Higgs couplings as dimensionless parameters are defined by

$$\begin{aligned} \mathcal{L}_{\text{tri}} = {} & \sum_{\varphi_0 = h,H} v \left\{ \frac{1}{3!} \hat{\lambda}_{\varphi_0\varphi_0\varphi_0} \varphi_0^3 + \frac{1}{2} \hat{\lambda}_{\varphi_0 AA} \varphi_0 A^2 \right. \\ & \left. + \lambda_{\varphi_0 H^+ H^-} \varphi_0 H^+ H^- \right\} + \frac{1}{2} \hat{\lambda}_{Hhh} v H h^2 + \frac{1}{2} \hat{\lambda}_{hHH} v h H^2. \end{aligned} \qquad (9)$$

In the inverted type I, the couplings are [47,48]

$$\begin{aligned} & \hat{\lambda}_{HHH} = -\frac{3m_{125}^2}{v^2}, \qquad \hat{\lambda}_{hHH} = 0, \\ & \hat{\lambda}_{hhh} = 3\hat{\lambda}_{hAA} = 3\hat{\lambda}_{hH^+H^-} = -\frac{3(M^2 - m_h^2)(t_\beta^2 - 1)}{t_\beta v^2}, \\ & \hat{\lambda}_{Hhh} = -\frac{m_{125}^2 + 2m_h^2 - 2M^2}{v^2}, \\ & \hat{\lambda}_{HAA} = -\frac{m_{125}^2 + 2M_A^2 - 2M^2}{v^2}, \\ & \hat{\lambda}_{HH^+H^-} = -\frac{m_{125}^2 + 2M_{H^\pm}^2 - 2M^2}{v^2}. \end{aligned} \qquad (10)$$

The Higgs alignment limit makes the trilinear coupling of the observed Higgs boson H the same as in the SM, $\hat{\lambda}_{HHH} \simeq 0.77$, which is one of the most important targets to measure at the High-Luminosity LHC (HL-LHC) and future colliders [49–54]. Another remarkable feature is that $\hat{\lambda}_{hhh}$, $\hat{\lambda}_{hAA}$, and $\hat{\lambda}_{hH^+H^-}$ have the common factor of $t_\beta(M^2 - m_h^2)$ in the large t_β limit.

III. SCANNING AND RGE ANALYSIS

Before studying the high-energy behavior of the model via RGEs, the preparation of the allowed parameter points at the electroweak scale is an essential prerequisite.

Therefore, we randomly scan five model parameters in the range of

$$t_\beta \in [1, 50], \qquad M_A \in [10, 3000]\ \text{GeV},$$
$$m_{12}^2 \in [-3000^2, 3000^2]\ \text{GeV}^2,$$
$$M_{H^\pm} \in [80, 3000]\ \text{GeV}, \qquad m_h \in [10, 120]\ \text{GeV} \tag{11}$$

and cumulatively impose the following constraints:

(i) Theoretical requirements: We demand the bounded-from-below Higgs potential [55], tree-level unitarity of scalar-scalar scatterings [41,56–58], perturbativity [39], and the stability of the CP-conserving vacuum with $v = 246$ GeV [59–61]. We use the public code 2HDMC v1.8.0 [62]. For the perturbativity, 2HDMC requires that the magnitudes of all the quartic couplings among physical Higgs bosons be less than 4π. However, 2HDMC does not check whether our vacuum is the global minimum of the potential. We demand the tree-level vacuum stability condition of [61]

$$m_{12}^2(m_{11}^2 - k^2 m_{22}^2)(t_\beta - k) > 0, \tag{12}$$

where $k = (\lambda_1/\lambda_2)^{1/4}$. The tree-level conditions have been known to be more than sufficient up to very high scales in the Higgs alignment limit [30,63].

(ii) Peskin-Takeuchi oblique parameters [64]: The oblique parameters of S, T, and U in the 2HDM [65–67] should satisfy the current best-fit results at 95% C.L. [68],

$$S = -0.02 \pm 0.10,$$
$$T = 0.03 \pm 0.12, \qquad U = 0.01 \pm 0.11,$$
$$\rho_{ST} = 0.92, \qquad \rho_{SU} = -0.80, \qquad \rho_{TU} = -0.93, \tag{13}$$

where ρ_{ij} is the correlation matrix.

(iii) Flavor-changing neutral currents: We demand that the most recent observables from B physics be satisfied at 95% C.L. [69–71]. We adopt the results of Ref. [69].

(iv) Higgs precision data: We use the public code HiggsSignals v2.6.2 [72] to check the consistency with the Higgs precision data. Based on the χ^2 value for 111 Higgs observables [73–80] with five parameters, we require that the p value be larger than 0.05.

(v) Direct search bounds: We demand that the model prediction to the cross sections of the direct search modes for new scalar bosons at the LEP, Tevatron, and LHC should be less than 95% C.L. upper bound on the observed cross sections. The open code HiggsBounds v5.10.2 [81] is used.

Brief comments on the recent collider detector at Fermilab (CDF) measurement of the W boson mass [82], $m_W^{\text{CDF}} = 80.4335 \pm 0.0094$ GeV, are in order here. If we accept m_W^{CDF}, the oblique parameters change into $S_{\text{CDF}} = 0.15 \pm 0.08$ and $T_{\text{CDF}} = 0.27 \pm 0.06$ with $U = 0$ [83]. Although m_W^{CDF} has important implications on the 2HDM [35,36,83–96], our main conclusion on the role of trilinear Higgs couplings in disentangling the high- and low-cutoff scales does not change. Therefore, we focus on the oblique parameters without the CDF m_W measurement.

Over the parameter points that pass the above constraints, we evolve the following parameters via the RGE, by using the public code 2HDME [32,97]:

$$g_{1,2,3}, \quad \lambda_{1,\ldots,5}, \quad \xi_f^{h,H,A}, \quad m_{11}, \quad m_{12}, \quad m_{22}^2, \quad v_{1,2}. \tag{14}$$

We include the mixing effects of two scalar doublet fields (with equal quantum numbers) on v_1 and v_2, which bring about the RG running of t_β. The top quark pole mass scale, $m_t^{\text{pole}} = 173.4$ GeV, is used to match the 2HDM to the SM. The boundary conditions at m_t^{pole} are referred to Ref. [32]. The β functions of the gauge, Yukawa, and quartic couplings at one-loop level are presented in the Appendix. Since the difference between the one- and two-loop RG running is not large,[2] we take the one-loop RGE to efficiently cover all the parameter points.

Now let us describe how we obtained the cutoff scale Λ_{cut}. For each parameter point, we perform the RGE evolution up to the next high-energy scale[3] and check three conditions: tree-level unitarity, perturbativity, and vacuum stability.[4] If all three are satisfied, we increase the energy scale into the next step. If any condition is violated, we stop the running and record the energy scale as Λ_{cut}. We find that the Landau pole appears at a higher scale than Λ_{cut}. We additionally require that the cutoff scale should be larger than 1 TeV. In what follows, the "viable parameter points" denote the parameter points that satisfy the aforementioned constraints and $\Lambda_{\text{cut}} > 1$ TeV.

Strong correlations exist between the cutoff scale and the model parameters. In Fig. 2, we present the viable parameter points over the plane of $(M_A, M_{H^\pm})$ in the left panel and (m_h, t_β) in the right panel. The color code denotes the cutoff scale Λ_{cut}. We sorted the parameter points according to Λ_{cut} and stacked them in order of Λ_{cut}, the points with low Λ_{cut} underneath and those with high Λ_{cut} on top.

---

[2] For randomly selected parameter points, we compared Λ_{cut} at one-loop level with Λ_{cut} at two-loop level. The difference is $\mathcal{O}(10)\%$.

[3] To cover from the electroweak scale to the Planck scale, we take a uniform step in $\log(Q)$.

[4] Note that 2HDME uses the perturbativity condition of $|\lambda_{1,\ldots,5}| < 4\pi$ and the tree-level vacuum stability conditions in Refs. [55,98].

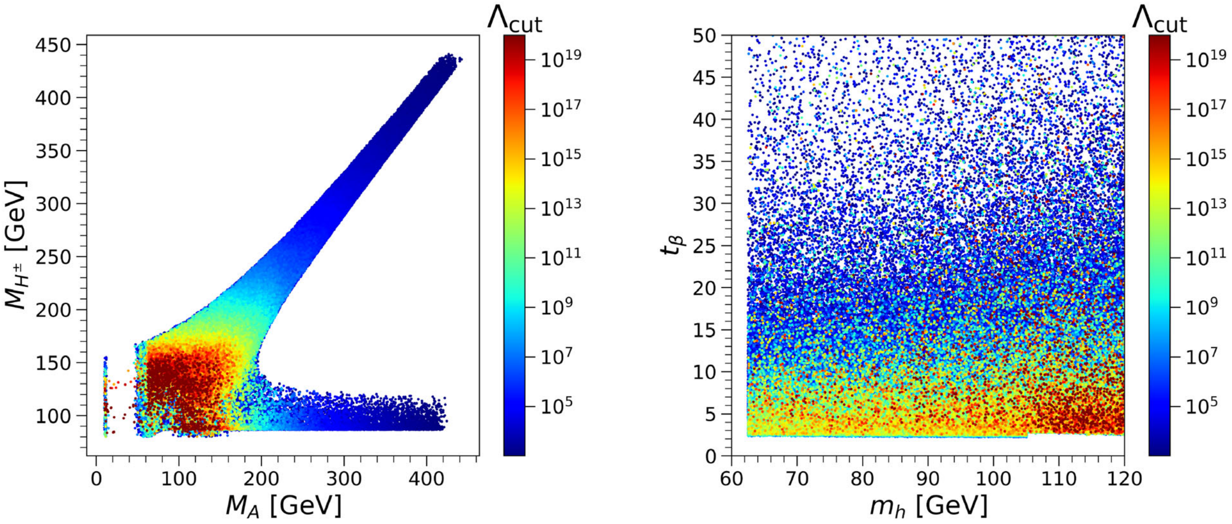

FIG. 2. $M_{H^\pm}$ versus M_A (left) and t_β versus m_h (right). The color code denotes the cutoff scale $\Lambda_{\rm cut}$.

The overlap is due to the projection of five-dimensional parameter space in Eq. (5) on a two-dimensional subspace.

Several remarkable features are shown in Fig. 2. First, the viable parameter points are pretty limited even with the weak condition of $\Lambda_{\rm cut} > 1$ TeV. The upper bounds on M_A and $M_{H^\pm}$ exist as $M_A, M_{H^\pm} \lesssim 430$ GeV, to which the condition of $\Lambda_{\rm cut} > 1$ TeV plays a critical role. The Peskin-Takeuchi oblique parameter T is satisfied if $M_{H^\pm} \sim M_A$ or $M_{H^\pm} \sim m_h$, which explains two branches in the left panel of Fig. 2. The lower branch corresponds to $M_{H^\pm} \sim m_h$, which puts the upper bound on the charged Higgs boson mass. For the intermediate mass range of $M_A, M_{H^\pm} \lesssim 200$ GeV, there is no particular correlation between M_A and $M_{H^\pm}$. However, meaningful correlations appear outside the box with $M_A, M_{H^\pm} \lesssim 200$ GeV. If $M_{H^\pm} \gtrsim 200$ GeV (belonging to the upper branch), $M_{H^\pm} \simeq M_A$. If $M_{H^\pm} \lesssim 200$ GeV and $M_A \gtrsim 200$ GeV (belonging to the lower branch), $M_{H^\pm} \sim 100$ GeV. The lighter CP-even Higgs boson mass m_h (right panel of Fig. 2) is heavier than half the observed Higgs boson mass due to the strong constraint from the exotic Higgs boson decay of $H \to hh$. For t_β, most values in the scanning are permitted. Although the density of the allowed t_β in the scatter plot is lower for larger t_β, we cannot conclude that large t_β is disfavored: nature chooses just one parameter point.

The second remarkable feature of Fig. 2 is that substantial parameter points in the inverted type I remain stable all the way up to the Planck scale. Let us investigate the characteristics of the parameter points with the high-cutoff scale. In Fig. 3, we show M_A versus m_h (left panel) and t_β versus M^2 (right panel) after imposing $\Lambda_{\rm cut} > 10^{18}$ GeV. The color code in the left (right) panel denotes $M_{H^\pm}$ (m_h).

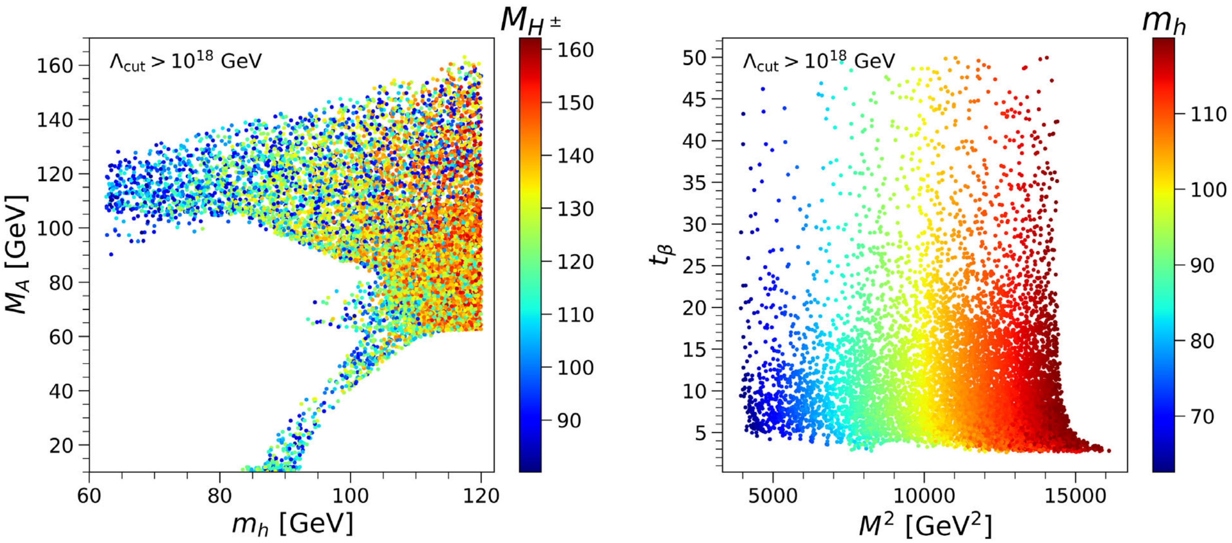

FIG. 3. For $\Lambda_{\rm cut} > 10^{18}$ GeV, M_A versus m_h (left) and t_β versus M^2 (right). The color code denotes $M_{H^\pm}$ (left) and m_h (right).

It is clearly seen that the high-cutoff scale requires *light* masses of the extra Higgs bosons like $M_A, M_{H^\pm} \lesssim 160$ GeV. We observe that the charged Higgs boson is lighter than the top quark for the Planck-scale cutoff. However, the lower bounds of $M_A \gtrsim 10$ GeV, $m_h \gtrsim 62.5$ GeV, and $M_{H^\pm} \gtrsim 80$ GeV do not change by imposing $\Lambda_{\rm cut} > 10^{18}$ GeV. Similarly, the Planck-scale cutoff does not affect the values of t_β, as shown in the right panel of Fig. 3.

The values of M^2 are also limited even with $\Lambda_{\rm cut} > 1$ TeV. Only the positive values of M^2 are permitted because negative M^2 enhances λ_1 through the terms proportional to t_β^2. Large λ_1 at the electroweak scale quickly evolves into an unacceptably large value, which endangers the global minimum condition of the vacuum [59–61]. For $\Lambda_{\rm cut} > 10^{18}$ GeV, a unique correlation of $M^2 \simeq m_h^2$ appears, as shown in the right panel in Fig. 3. It is also ascribed to the t_β^2 terms in λ_1. The condition of $M^2 \simeq m_h^2$ suppresses the t_β^2 terms and thus helps to retain the stability of the scalar potential.

Although the high-cutoff scale demands light masses of the extra Higgs bosons, the inverse is not true. All the mass spectra in the left panel of Fig. 3 also accommodate a low-cutoff scale; see Fig. 1. Even if we observe $m_h = M_A = 100$ GeV and $M_{H^\pm} = 140$ GeV, for example, the mass spectrum alone cannot tell whether the cutoff scale is high or low. The reader may suggest to use t_β as a discriminator of the cutoff scale. However, measuring t_β in type I is challenging at the LHC, especially when $t_\beta \gg 1$. The value of t_β governs the fermionic productions (from the top quark decay or gluon fusion via quark loops) and fermionic decays of the extra Higgs bosons. If t_β is large, the fermionic production of the extra Higgs bosons is highly suppressed because all the Yukawa couplings of the extra Higgs bosons are inversely proportional to t_β in type I. The bosonic productions such as $q\bar{q} \to Z^* \to Ah$ and $q\bar{q} \to W^* \to H^\pm h/A$ [37,99–109] do not give information about t_β. Moreover, the fermionic decay parts are insensitive to t_β because of the same dependence of all the Yukawa couplings on t_β. If we cannot measure the exact value of large t_β, it is reasonable to include all the viable parameter points with $t_\beta > 10$ when pursuing a way to discriminate the high and low $\Lambda_{\rm cut}$.

IV. TRILINEAR HIGGS COUPLINGS

In this section, we study the trilinear Higgs couplings to measure $\Lambda_{\rm cut}$. We consider the following three benchmark points (BPs):

$$\begin{aligned}
&\text{BP-1}: m_h = 70\ \text{GeV}, \quad M_A = 110\ \text{GeV}, \quad M_{H^\pm} = 110\ \text{GeV},\\
&\text{BP-2}: m_h = 100\ \text{GeV}, \quad M_A = 100\ \text{GeV}, \quad M_{H^\pm} = 140\ \text{GeV},\\
&\text{BP-3}: m_h = 110\ \text{GeV}, \quad M_A = 70\ \text{GeV}, \quad M_{H^\pm} = 140\ \text{GeV},
\end{aligned} \tag{15}$$

all of which accommodate the cutoff scale from 1 TeV to 10^{19} GeV. As discussed in the previous section, we focus on the large t_β limit as

$$\text{Large}\ t_\beta\ \text{case}: \ t_\beta > 10. \tag{16}$$

For m_{12}^2, we incorporate all the values that satisfy the constraints in Sec. III.

Let us turn to the trilinear Higgs couplings versus $\Lambda_{\rm cut}$. In Fig. 4, we present $\hat{\lambda}_{hhh}$ (left panel), $\hat{\lambda}_{Hhh}$ (middle panel), and $\hat{\lambda}_{HH^+H^-}$ (right panel) at the electroweak scale, as a function of $\Lambda_{\rm cut}$: note that $\hat{\lambda}_{hAA} = \hat{\lambda}_{hH^+H^-} = \hat{\lambda}_{hhh}/3$. Here only the BP-2 results are shown because BP-1 and BP-3 yield similar results with $\mathcal{O}(10)\%$ differences. The value of t_β is shown via the color code. It is impressive that the values of $\hat{\lambda}_{hhh}$, $\hat{\lambda}_{Hhh}$, and $\hat{\lambda}_{HH^+H^-}$ for $\Lambda_{\rm cut} = 10^{18}$ GeV are not overlapped with those for $\Lambda_{\rm cut} \lesssim 10^{17}$ GeV, although the allowed values for lower $\Lambda_{\rm cut}$ are considerably spread by the unfixed t_β and m_{12}^2. The most sensitive dependence on $\Lambda_{\rm cut}$ is shown in $\hat{\lambda}_{hhh}$, which ranges in $[-0.09, 1.1]$. Since $\hat{\lambda}_{hhh} = 0$ is included, the

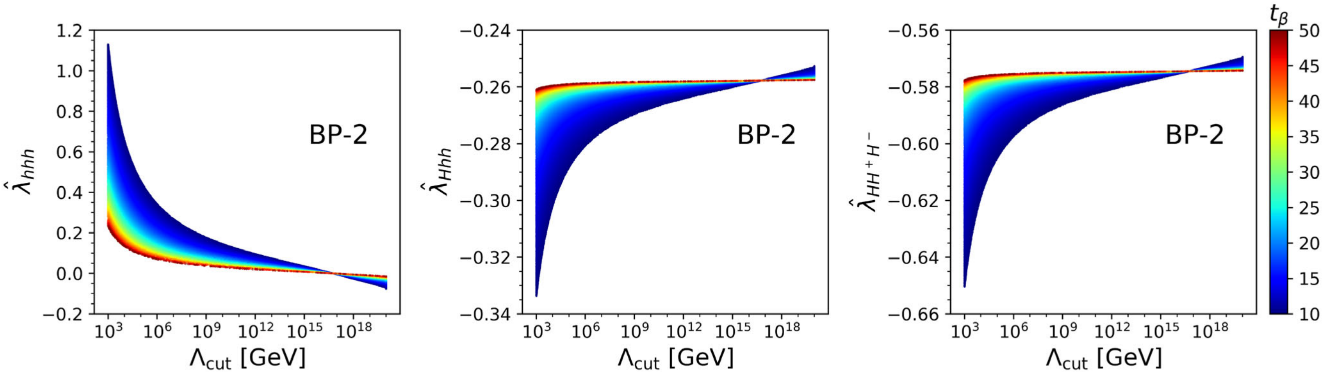

FIG. 4. Trilinear Higgs couplings of $\hat{\lambda}_{hhh}$ (left), $\hat{\lambda}_{Hhh}$ (middle), and $\hat{\lambda}_{HH^+H^-}$ (right) against the cutoff scale $\Lambda_{\rm cut}$. The color code denotes t_β. We take BP-2 where $m_h = M_A = 100$ GeV, $M_{H^\pm} = 140$ GeV, and $t_\beta > 10$.

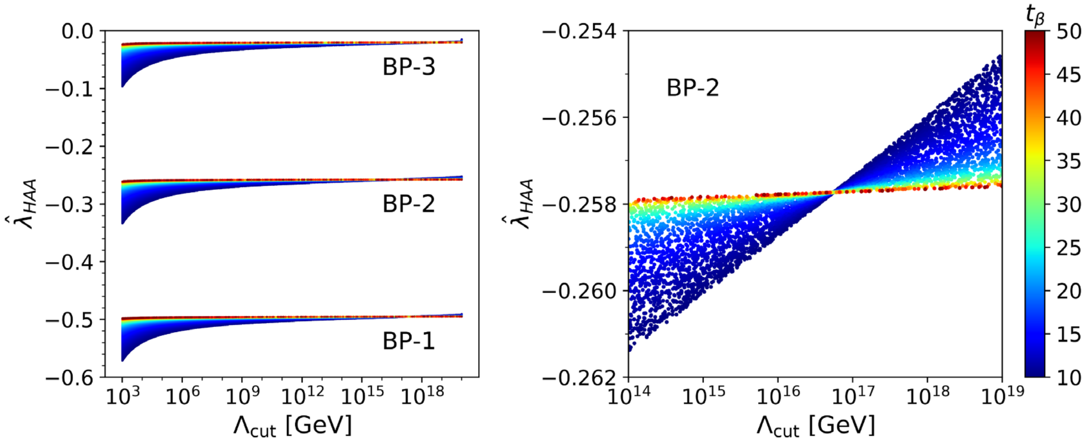

FIG. 5. Trilinear Higgs couplings of $\hat{\lambda}_{HAA}$ versus the cutoff scale $\Lambda_{\rm cut}$ for BP-1, BP-2, and BP-3 (left) and $\hat{\lambda}_{HAA}$ around the *focus* cutoff scale for BP-2 (right). The color code denotes t_β. We include all the viable parameter points with $t_\beta > 10$.

change of $\hat{\lambda}_{hhh}$ according to $\Lambda_{\rm cut}$ is huge. On the other hand, the variations of $\hat{\lambda}_{Hhh}$ and $\hat{\lambda}_{HH^+H^-}$ are small within $10\% \sim 20\%$.

In the left panel of Fig. 5, we present $\hat{\lambda}_{HAA}$ versus $\Lambda_{\rm cut}$ for BP-1, BP-2, and BP-3. Unlike $\hat{\lambda}_{hhh}$, $\hat{\lambda}_{Hhh}$, and $\hat{\lambda}_{HH^+H^-}$, the value of $\hat{\lambda}_{HAA}$ is sensitive to the benchmark point. For high $\Lambda_{\rm cut}$, $|\hat{\lambda}_{HAA}|$ of BP-1 is about 25 times larger than that of BP-3. $\hat{\lambda}_{HAA}$ depends on M_A and M^2, not on t_β. Since $M^2 \approx m_h^2$ and $m_h \sim m_{125}$ as shown in Fig. 3, the M^2 contribution to $\hat{\lambda}_{HAA}$ is nearly canceled by the m_{125} contribution. So, the heavier M_A is, the larger $|\hat{\lambda}_{HAA}|$ is.

We observe a special $\Lambda_{\rm cut}$ in Fig. 4 and the right panel of Fig. 5. Around $\Lambda_{\rm cut} \simeq 10^{17}$ GeV, all the trilinear Higgs couplings are almost fixed. Even though we present only the results of BP-2 in Fig. 4, the same behavior is found in BP-1 and BP-3. The spread trilinear Higgs couplings are focused on a single cutoff point, which we call $\Lambda_{\rm cut}^{\rm focus}$. Since the allowed value of M^2 plays a crucial role in understanding $\Lambda_{\rm cut}^{\rm focus}$, we show $M(\equiv\sqrt{M^2})$ versus the cutoff scale $\Lambda_{\rm cut}$ for BP-2 in Fig. 6. The left panel presents the results of all the viable parameter points. It is clear to see that the parameter points with $\Lambda_{\rm cut} = \Lambda_{\rm cut}^{\rm focus}$ satisfy the condition of $M^2 = m_h^2$. We found that the reverse holds true. If we allow small deviation like $|M^2 - m_h^2| \leq 10\ {\rm GeV}^2$ as in the right panel of Fig. 6, the cutoff scale converges to $\Lambda_{\rm cut} = \Lambda_{\rm cut}^{\rm focus}$ for $t_\beta = 10$ but ranges from 10^{12} GeV to the Planck scale for $t_\beta = 50$. Then why does the condition of $M^2 = m_h^2$ fix the trilinear Higgs coupling? It is because the condition removes the t_β dependence of the trilinear couplings, which is the main source for their variation. In addition, $M^2 = m_h^2$ removes the dangerous t_β^2 terms of $\hat{\lambda}_1$, which guarantees the high-energy scale of $\Lambda_{\rm cut}^{\rm focus}$.

Now we discuss the other 2HDM scenarios. This paper concentrates on the inverted type I in the Higgs alignment limit. Let us first consider a small deviation from the alignment. Since the Higgs precision prospect at the future muon collider associated with the HL-LHC and the Higgs factory at $\sqrt{s} = 250$ GeV is $\delta\kappa_W \simeq 0.11\%$ [110], we consider two cases of $|s_{\beta-\alpha}| = 0.05,\ 0.1$. In Fig. 7, we present

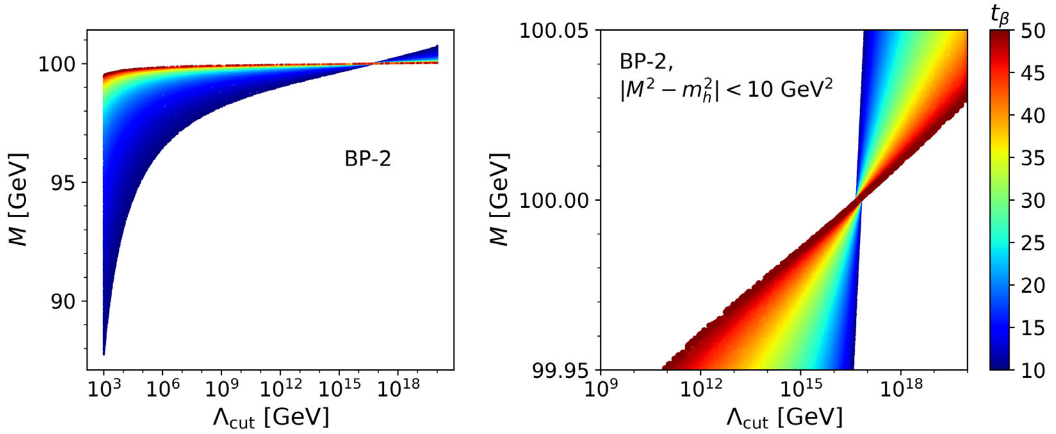

FIG. 6. $M(\equiv\sqrt{M^2})$ versus the cutoff scale $\Lambda_{\rm cut}$ for BP-2 with the color code of t_β. Left: results of all the viable parameter points. Right: those with $|M^2 - m_h^2| \leq 10\ {\rm GeV}^2$.

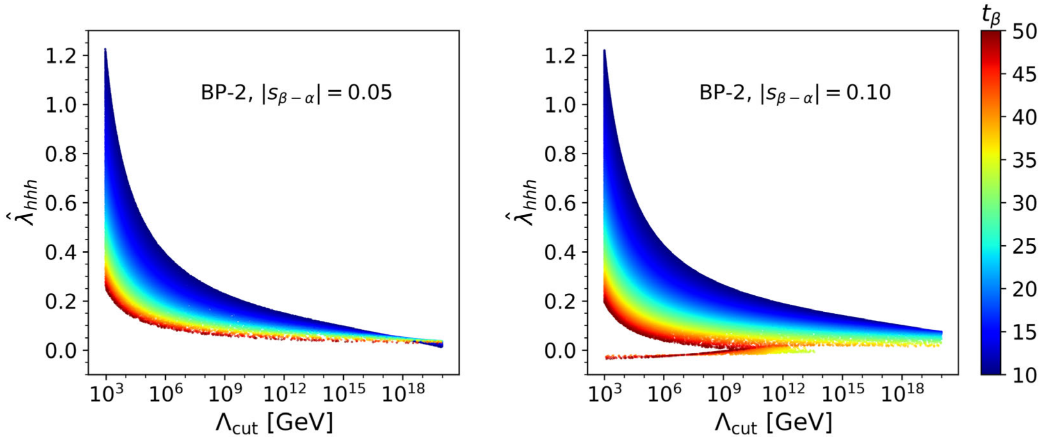

FIG. 7. For the small deviation from the Higgs alignment limit, $\hat{\lambda}_{hhh}$ versus the cutoff scale $\Lambda_{\rm cut}$ for BP-2 with the color code of t_β. Left: results of $|s_{\beta-\alpha}| = 0.05$. Right: results of $|s_{\beta-\alpha}| = 0.1$.

$\hat{\lambda}_{hhh}$ versus $\Lambda_{\rm cut}$ for $|s_{\beta-\alpha}| = 0.05$ (left panel) and $|s_{\beta-\alpha}| = 0.1$ (right panel). Here only BP-2 results are shown. For $|s_{\beta-\alpha}| = 0.05$, the behavior of $\hat{\lambda}_{hhh}$ about $\Lambda_{\rm cut}$ remains almost same as the alignment case. The values of $\hat{\lambda}_{hhh}$ for $\Lambda_{\rm cut} = 10^{18}$ GeV are not overlapped with those for $\Lambda_{\rm cut} \lesssim 10^6$ GeV. If we increase the deviation from the alignment into $|s_{\beta-\alpha}| = 0.1$, the band of $\hat{\lambda}_{hhh}$ widens. The values of $\hat{\lambda}_{hhh}$ for $\Lambda_{\rm cut} = 10^{18}$ GeV are mostly overlapped with the low-cutoff scale, except for $\Lambda_{\rm cut} \lesssim 10$ TeV.

Finally, we discuss whether we have similar results for other types or the normal Higgs scenario where the lighter *CP*-even Higgs boson is the observed one. In the inverted Higgs scenario, type II and type Y are excluded by imposing the condition of $\Lambda_{\rm cut} > 1$ TeV [35] because the constraint from $b \to s\gamma$, $M_{H^\pm} > 800$ GeV [111], contradicts the required light masses of the BSM Higgs bosons. Type X in the inverted scenario can accommodate $\Lambda_{\rm cut} = 10^{18}$ GeV and shows similar behaviors of the trilinear Higgs couplings about the cutoff scales. In the normal scenario, all four types can retain the theoretical stability up to $\Lambda_{\rm cut} = 10^{18}$ GeV. The high-cutoff scale demands the almost exact mass degeneracy among the BSM Higgs boson masses, i.e., $M = M_A = M_H = M_{H^\pm}$, but does not put any upper bounds on the masses. So, the question for the normal scenario is changed: how can we distinguish the high- and low-cutoff scales via observables if we observe a highly degenerate mass spectrum of the extra Higgs bosons? It is more challenging than in the inverted scenario due to the heavy masses and the soft decay products of the BSM Higgs bosons. Nevertheless, the similar behavior of $\hat{\lambda}_{HHH}$ about $\Lambda_{\rm cut}$ leaves a motivation for the phenomenological study in future colliders.

V. LHC PHENOMENOLOGY

For the LHC phenomenology, we first present the branching ratios of h (left panels), A (middle panels), and $H^\pm$ (right panels) as a function of $\Lambda_{\rm cut}$ in Fig. 8. The results of BP-1, BP-2, and BP-3 are in the upper, middle, and lower panels, respectively. We include all the viable parameter points. The first noteworthy feature in Fig. 8 is that the dominant decay mode of the extra Higgs boson with the given mass spectra is insensitive to the cutoff scale, even though the two parameters of $t_\beta(> 10)$ and m_{12}^2 are not fixed. The decay of h depends on the hierarchy between m_h and M_A. When $m_h \le M_A$ as in BP-1 and BP-2, the leading (next-to-leading) decay mode is $h \to bb$ ($h \to \tau^+\tau^-$). However, if $m_h > M_A$ as in BP-3, the dominant decay mode is $h \to AZ^*$. The suppressed Yukawa couplings of h by large t_β enhance the bosonic decay modes if kinematically open. The decay of A is primarily determined by the hierarchy between M_A and m_h. For BP-2 and BP-3 with $M_A \le m_h$, the pseudoscalar A dominantly decays into a pair of b quarks with $\mathrm{Br}(A \to b\bar{b}) \gtrsim 0.73$. The next-to-leading decay mode of A is into gg. The substantial $\mathrm{Br}(A \to gg)$ is attributed to the larger loop amplitudes of a pseudoscalar than those of a scalar for the spin-1/2 particle contributions [112]. The third one is $A \to \tau^+\tau^-$. If $M_A > m_h$ as in BP-1, however, $\mathrm{Br}(A \to hZ^*)$ becomes the largest, which holds for the entire range of $\Lambda_{\rm cut}$. The decay into $b\bar{b}$ is mostly the next-to-leading mode.[5]

The charged Higgs boson mainly decays into $hW^{\pm *}$ and $AW^{\pm *}$, for the three benchmark points. Once kinematically allowed, the bosonic decay modes are dominant: the $H^\pm$-$W^\mp$-h vertex is proportional to $c_{\beta-\alpha}(=1)$; the $H^\pm$-$W^\mp$-A vertex is originated from the pure gauge interaction. In BP-3 with $M_{H^\pm} > M_A$ and $M_{H^\pm} > m_h$, the branching ratios of the fermionic modes are below 1%. If either m_h or M_A is beyond the kinematic threshold as in BP-1 and BP-2, the fermionic decay modes become

---

[5] We caution the reader that the scattered points are overlapped except for the leading decay mode. For some parameter points, $A \to gg$ can be the next-to-leading mode.

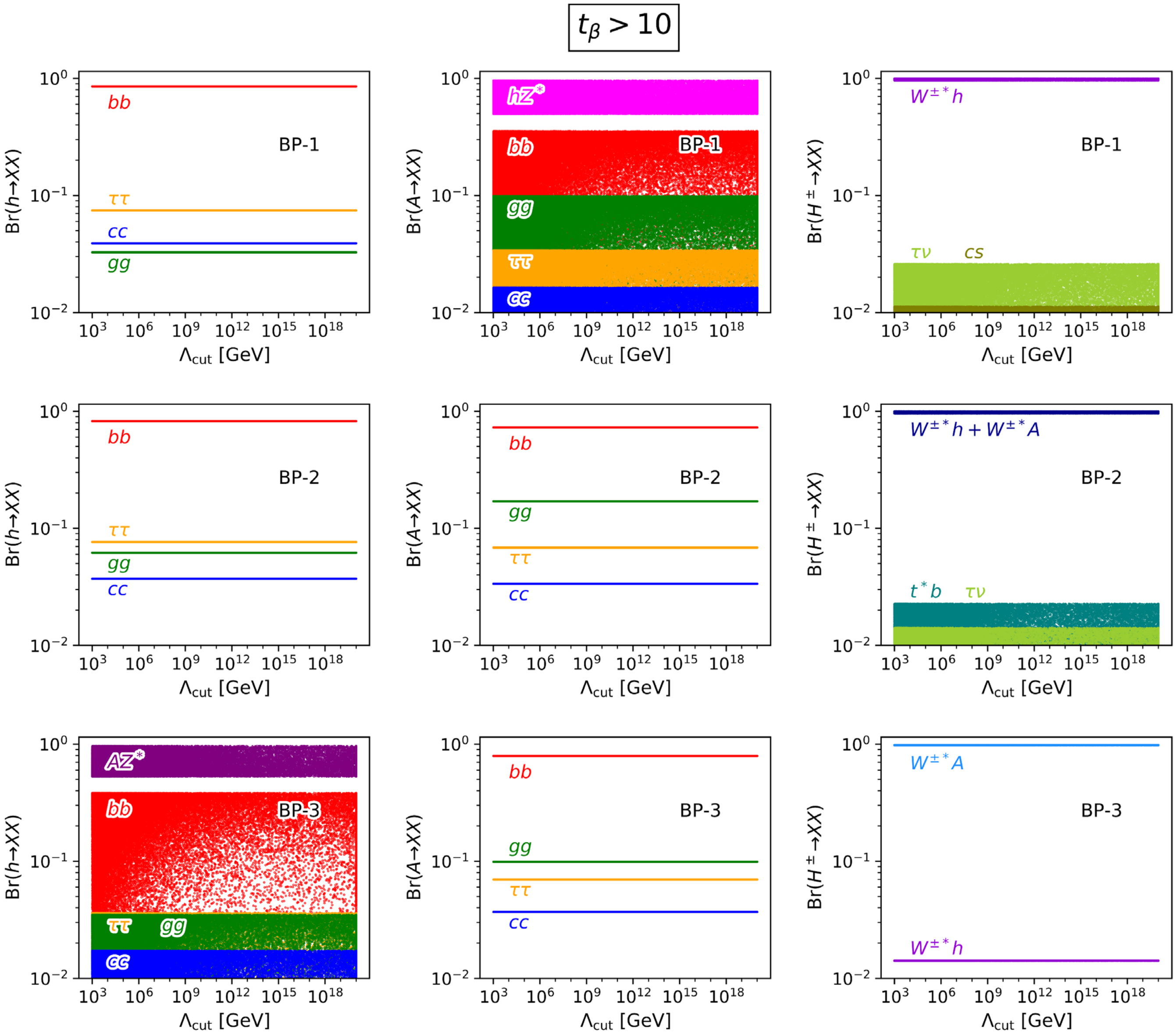

FIG. 8. Branching ratios of h (upper row), A (middle row), and $H^\pm$ (lower row) about the cutoff scale $\Lambda_{\rm cut}$. All the viable parameter points with $t_\beta > 10$ are included.

considerable. The leading fermionic decay mode depends on the charged Higgs bosons mass. For BP-1 where $M_{H^\pm}$ is substantially lighter than the top quark mass, $H^\pm \to \tau\nu$ has the largest branching ratio among the fermionic decay modes, followed by $H^\pm \to cs$. In BP-2 where $M_{H^\pm}$ is near to the top quark mass, $H^\pm \to t^* b$ becomes the leading fermionic mode, followed by $H^\pm \to \tau\nu$.

To probe the trilinear Higgs couplings at the LHC, we need to consider multi-Higgs production mediated by Higgs bosons. The first important production channels are the di-Higgs processes, $gg \to H/h \to hh/AA$. The corresponding Feynman diagram[6] is in the left panel of Fig. 9. The contribution of H destructively interferes with that of h because the signs of $\hat{\lambda}_{Hhh}$ and $\hat{\lambda}_{hhh}$ are opposite to each other; see Fig. 4.

In Fig. 10, we present as a function of $\Lambda_{\rm cut}$ the parton-level production cross sections for $gg \to hh$ (left panel) and $gg \to AA$ (right panel) at the 14 TeV LHC over the viable parameter points. All the three benchmark points in Eq. (15) are considered. The color code denotes t_β. To calculate the parton-level cross sections, we first obtained the Universal FeynRules Output (UFO) [113] by using FeynRules [114]. Then we interfered the UFO file with MadGraph5_aMC@NLO [115] and calculated the cross sections at the 14 TeV LHC with the NNPDF31_LO_AS_0118 parton distribution function set [116].

---

[6] We omit the box diagrams from the top quark loop because two factors of $1/t_\beta$ suppress them.

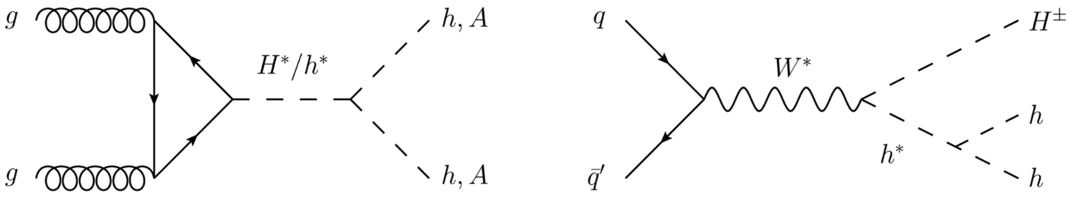

FIG. 9. Feynman diagrams of $gg \to hh/AA$ (left) and $q\bar{q}' \to W^* \to H^\pm hh$ (right).

For the production cross sections of $gg \to hh$, the most crucial factor is m_h. The lighter m_h is, the larger $\sigma(gg \to hh)$ is. BP-1 yields the largest cross section. On the contrary, the production cross section of $gg \to AA$ is larger for heavier M_A. The BP-1, which has the heaviest M_A among the three benchmark points, has the largest cross section. It seems contradictory to the kinematic loss by the heavy M_A. The main reason is that the dominant contribution to $gg \to AA$ is from H and thus $\hat{\lambda}_{HAA}$ determines the signal rate. The heavier M_A is, the larger $\hat{\lambda}_{HAA}$ is; see Fig. 5.

The dependence of $\sigma(gg \to hh/AA)$ on $\Lambda_{\rm cut}$ is not large enough to distinguish the high- and low-cutoff scales. Even the optimistic case, the process of $gg \to hh$ in BP-1 with $t_\beta = 10$, makes a few femtobarn difference in the cross sections between $\Lambda_{\rm cut} = 1$ TeV and $\Lambda_{\rm cut} = 10^{18}$ GeV. It is too small to probe at the HL-LHC with the expected total luminosity of 3 ab^{-1}. For larger t_β like 50, the di-Higgs production cross sections become more insensitive to $\Lambda_{\rm cut}$. The weak dependence of $\sigma(gg \to hh)$ on $\Lambda_{\rm cut}$ is due to the dominant contribution from H and the destructive interference between the H and h contributions. In the BP-1 with $t_\beta = 10$ and $\Lambda_{\rm cut} = 1$ TeV, for example, the cross section from H alone is $\sigma(gg \to H \to hh) \simeq 36.5$ fb, from h alone is $\sigma(gg \to h \to hh) \simeq 1.1$ fb, and from the interference $\sigma(gg \to hh)_{\rm intf} \simeq -12.1$ fb. The $\hat{\lambda}_{Hhh}$ controls the cross section, but its variation about $\Lambda_{\rm cut}$ is small.

To single out only one trilinear Higgs coupling, we consider triple Higgs productions at the LHC. Since the gluon fusion production of the tri-Higgs process through the top quark loop is suppressed by large t_β, we concentrate on the tri-Higgs productions mediated by the gauge bosons. Through the Z boson, we have

$$q\bar{q} \to Z^* \to Ah^* \to Ahh, \qquad q\bar{q} \to Z^* \to A^*h \to Ahh, \tag{17}$$

$$q\bar{q} \to Z^* \to Ah^* \to AAA, \tag{18}$$

and through W,

$$q\bar{q}' \to W^* \to H^\pm h^* \to H^\pm hh, \tag{19}$$

$$q\bar{q}' \to W^* \to H^\pm h^* \to H^\pm AA, \tag{20}$$

$$q\bar{q}' \to W^* \to H^\pm A^* \to H^\pm Ah. \tag{21}$$

As a representative, we present the Feynman diagram of $q\bar{q}' \to H^\pm hh$ in the right panel of Fig. 9. Since all the above processes in Eqs. (17)–(21) have the same topology of the Feynman diagram, the production cross sections as a

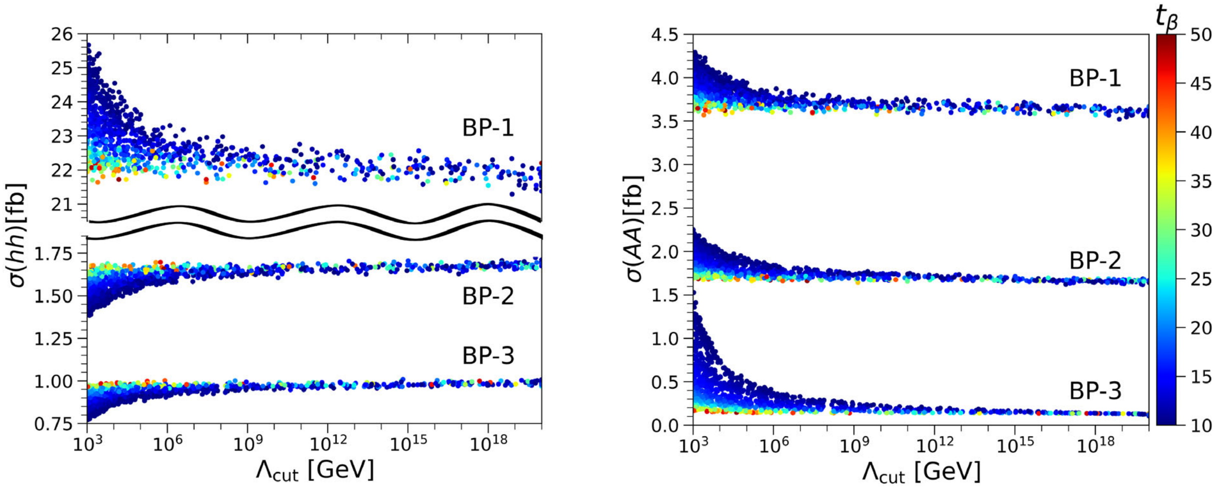

FIG. 10. Cross sections of $gg \to hh$ (left) and $gg \to AA$ (right) at the 14 TeV LHC, as a function of $\Lambda_{\rm cut}$. The color code denotes t_β. The description of the benchmarks is in the main text.

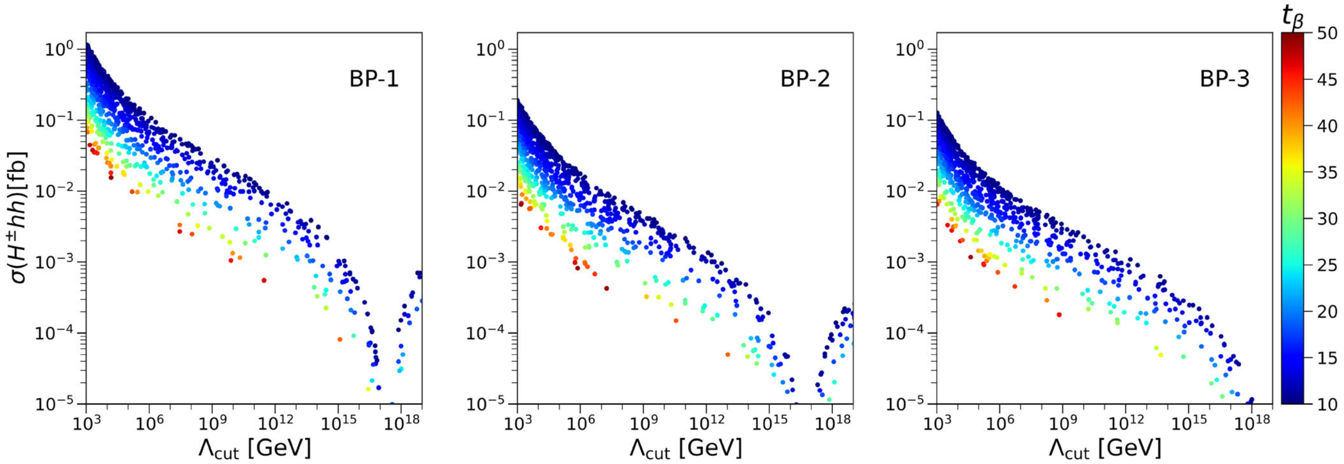

FIG. 11. Cross sections of $q\bar{q}' \to H^\pm hh$ at the 14 TeV LHC as a function of $\Lambda_{\rm cut}$, for BP-1 (left), BP-2 (middle), and BP-3 (right). The color codes indicate t_β.

function of $\Lambda_{\rm cut}$ show almost the same behavior. In BP-2, for example, $\sigma(pp \to Ahh)/\sigma(pp \to H^\pm hh) \simeq 0.9$ holds for all $\Lambda_{\rm cut}$.

In Fig. 11, we present the parton-level production cross sections of $q\bar{q}' \to H^\pm hh$ at the 14 TeV LHC for BP-1 (left panel), BP-2 (middle panel), and BP-3 (right panel). The color code denotes t_β. The difference of the cross section according to $\Lambda_{\rm cut}$ is big enough to distinguish the high- and low-cutoff scales of the inverted type I. The ratio of the cross section for $\Lambda_{\rm cut} = 1$ TeV to that for $\Lambda_{\rm cut} = 10^{18}$ GeV is more than about 10^3. This is the most remarkable result of our study. Measuring the signal rate of the triple Higgs production tells whether the cutoff scale is high or low.

Finally, we discuss the discovery potential at the HL-LHC. Discriminating the high- and low-cutoff scales through $gg \to hh/AA$ requires the precision measurement on the cross section within $\sim$1 fb. Let us roughly estimate the feasibility. The processes of $gg \to hh$ and $gg \to AA$ mainly yield $4b$ final states because $A/h \to bb$ is leading or next-to-leading. Resembling the di-Higgs process in the SM, they are challenging to observe for two reasons. First, the cross section itself is too small. The maximum cross section, which happens for $\Lambda_{\rm cut} = 1$ TeV, reaches $\mathcal{O}(10)$ fb. It is to be compared with the SM leading-order result of $\sigma(gg \to h_{\rm SM}h_{\rm SM})_{\rm LO} \simeq 17$ fb at $\sqrt{s} = 14$ TeV [117]. Since the projected signal significance of the SM Higgs boson pair production at the HL-LHC with the total luminosity of 3 ab^{-1} is 3.0σ, when the $bbbb$, $bb\tau^+\tau^-$, and $bb\gamma\gamma$ decay channels are all combined [118], it is hard to observe $gg \to hh/AA$. The second difficulty comes from the softer b jets than in the SM di-Higgs process. For $gg \to hh \to 4b$, the lighter m_h than 125 GeV yields soft b quarks. For $gg \to AA \to 4b$, most of the viable parameter points in Fig. 3 have $M_A < 125$ GeV, which generate soft b quarks. As the b tagging efficiency is reduced, the signal significance decreases as well. In summary, the di-Higgs process is not efficient to probe the cutoff scale.

The triple Higgs production of $H^\pm hh$ has higher discovery potential. Since the charged Higgs boson mainly decays into $W^{\pm *}A/h$ in the three benchmark points, followed by $h/A \to bb$, the final state is $6b + \ell\nu$. This attractive channel has not been studied in the literature.[7] The main backgrounds are

$$\begin{aligned} &t+\bar{t}+\ell\nu \to b j_b^{\rm mis} j_b^{\rm mis} + b j_b^{\rm mis} j_b^{\rm mis} + \ell\nu, \\ &t+\bar{t}+jj \to b\ell\nu + b j_b^{\rm mis} j_b^{\rm mis} + j_b^{\rm mis} j_b^{\rm mis}, \end{aligned} \tag{22}$$

where $j_b^{\rm mis}$ is the light jet (from u, d, s, c, and g) mistagged as a b quark jet. We calculated the parton-level cross sections of the backgrounds, with the b tagging and mistagging efficiencies of $P_{b\to b} = 0.7$, $P_{c\to b} = 0.05$, and $P_{j\to b} = 0.01$. We imposed the selection cuts of $p_T^b > 20$ GeV, $p_T^\ell > 10$ GeV, $|\eta^{\ell,j}| < 2.5$, $E_T^{\rm miss} > 20$ GeV, and the separation $\Delta R_{ii'} > 0.4$. After the basic selection, the background cross section from $t\bar{t}jj$ is about 8.7 ab and from $t\bar{t}\ell\nu$ is about 3.8×10^{-4} ab. If we impose additional cuts on the invariant mass of two b jets like $|m_{bb} - m_h| < 15$ GeV, the backgrounds are negligible. Despite the almost background-free environment, the high $\Lambda_{\rm cut}$ yields too small signal rate of $pp \to H^\pm hh$ at the 14 TeV LHC.

Exploring the cutoff scale in the inverted type I via the $6b + \ell\nu$ final state has a better chance in future high-energy colliders such as the Future Hadron-Hadron Circular Collider (FCC-hh) at CERN [121], the CEPC [122,123], and the muon collider [124–126]. Particularly, we have high expectations for the muon collider with benchmark energies in the range of $\sqrt{s} = 3$–30 TeV and the integrated luminosity of $\mathcal{L} = 10(\sqrt{s}/10\ \text{TeV})^2$ ab^{-1}. The triple Higgs processes in Eqs. (17) and (18) with $q\bar{q}$ replaced

---

[7] The final state of $4j + \ell\nu$ was studied for the vector boson scattering of $WW \to WW$ [119], and the SM Higgs boson decaying into a fat jet consisting of $4b/6b/8b$ was studied [120].

by $\mu^+\mu^-$ will be able to disentangle the high- and low-cutoff scales in the inverted type I.

VI. CONCLUSION

Beyond the studies on how high the cutoff scale of a new physics model can go up, we have pursued an efficient observable to distinguish the high- and low-cutoff scales. The type I in the 2HDM has been considered for the inverted scenario where the observed Higgs boson at a mass of 125 GeV is the heavier CP-even Higgs boson H. We have first obtained the still-available parameter points that satisfy the theoretical requirements, the experimental constraints, and the cutoff scale above 1 TeV. The viable parameter space at the electroweak scale is already limited such that $M_A, M_{H^\pm} \lesssim 430$ GeV and $m_h \gtrsim 62.5$ GeV. Through the calculation of the cutoff scale $\Lambda_{\rm cut}$ of each viable parameter point by using the RGE, we have shown that the inverted type I can retain the stability all the way up to the Planck scale.

The condition of $\Lambda_{\rm cut} > 10^{18}$ GeV requires the light masses of the extra Higgs bosons like $M_A, M_{H^\pm} \lesssim 160$ GeV. However, the light masses alone cannot guarantee the high-cutoff scale because the parameter points with light masses accommodate $\Lambda_{\rm cut}$ from 1 TeV to 10^{19} GeV. Targeting at the phenomenologically challenging case of $t_\beta > 10$, we have investigated the trilinear Higgs couplings versus $\Lambda_{\rm cut}$. Although the values of all the trilinear couplings for $\Lambda_{\rm cut} = 1$ TeV are different from those for $\Lambda_{\rm cut} = 10^{18}$ GeV, $\hat{\lambda}_{hhh}$ shows a large variation about $\Lambda_{\rm cut}$, $\hat{\lambda}_{hhh} \in [-0.09, 1.1]$. Multi-Higgs boson productions at the LHC have been studied to probe the cutoff scale. The gluon fusion productions of the di-Higgs, $gg \to hh/AA$, are not efficient to measure $\hat{\lambda}_{hhh}$ because the dominant contribution from H dilutes the h contribution. The most remarkable result is in the tri-Higgs process of $pp \to H^\pm hh$ mediated by the W boson. The signal cross section shows huge variation according to $\Lambda_{\rm cut}$, like $\sigma_{\Lambda_{\rm cut}=1\ {\rm TeV}}/\sigma_{\Lambda_{\rm cut}=10^{18}\ {\rm GeV}} \sim 10^3$. The precision measurement of $pp \to H^\pm hh$ can indeed distinguish the high- and low-cutoff scales of the model. Considering the dominant decay modes of $H^\pm \to W^{\pm *}A/h$, $h \to bb$, and $A \to bb$, an efficient final state of $pp \to H^\pm hh$ is $6b + \ell\nu$. Although it enjoys an almost background-free environment at the LHC, the small cross section ($\lesssim 1$ ab) for $\Lambda_{\rm cut} = 10^{18}$ GeV motivates future high-energy colliders, especially the muon collider with $\sqrt{s} = 3$–30 TeV.

ACKNOWLEDGMENTS

The work of J. K., S. L, and J. S. is supported by the National Research Foundation of Korea, Grant No. NRF-2022R1A2C1007583. S. K. K. was supported by the National Research Foundation of Korea (NRF) grant funded by the Korea government (MSIT) (No. 2019R1A2C1088953).

APPENDIX: RGEs IN THE TYPE I

Focusing on the type I, we present the one-loop level RGEs [26,30,41,127,128]. The beta functions of gauge couplings are given by

$$16\pi^2\beta_{g_3} = -7g_3^3, \tag{A1}$$

$$16\pi^2\beta_{g_2} = \left(-\frac{10}{3} + \frac{n_d}{6}\right)g_2^3 = -3g_2^3, \tag{A2}$$

$$16\pi^2\beta_{g_1} = \left(\frac{20}{3} + \frac{n_d}{6}\right) = 7g_1^3, \tag{A3}$$

where n_d is the number of the scalar doublets of the fermions, so $n_d = 2$ in the 2HDM. The running of the quartic couplings of λ_i's is different according to the type. First, we write the β functions in terms of the common part c_i and the type-dependent part h_i as

$$16\pi^2\beta_{\lambda_i}^{\rm type} = c_i + h_i^{\rm type}, \qquad (i = 1, \ldots, 5). \tag{A4}$$

The common parts for λ_i's are

$$\begin{aligned}
c_1 &= 12\lambda_1^2 + 4\lambda_3^2 + 4\lambda_3\lambda_4 + 2\lambda_4^2 + 2\lambda_5^2 + \frac{3}{4}(3g^4 + g'^4 + 2g^2g'^2) - 3\lambda_1(3g^2 + g'^2),\\
c_2 &= 12\lambda_2^2 + 4\lambda_3^2 + 4\lambda_3\lambda_4 + 2\lambda_4^2 + 2\lambda_5^2 + \frac{3}{4}(3g^4 + g^4 + 2g^2g'^2) - 3\lambda_2(3g^2 + g'^2) + 12y_t^2\lambda_2 - 12y_t^4,\\
c_3 &= (\lambda_1 + \lambda_2)(6\lambda_3 + 2\lambda_4) + 4\lambda_3^2 + 2\lambda_4^2 + 2\lambda_5^2 + \frac{3}{4}(3g^4 + g'^4 - 2g^2g'^2) - 3\lambda_3(3g^2 + g'^2) + 2(3y_t^2 + 3y_b^2 + y_\tau^2)\lambda_3,\\
c_4 &= 2(\lambda_1 + \lambda_2)\lambda_4 + 8\lambda_3\lambda_4 + 4\lambda_4^2 + 8\lambda_5^2 + 3g^2g'^2 - 3(3g^2 + g'^2)\lambda_4 + 2(3y_t^2 + 3y_b^2 + y_\tau^2)\lambda_4,\\
c_5 &= 2(\lambda_1 + \lambda_2 + 4\lambda_3 + 6\lambda_4)\lambda_5 - 3\lambda_5(3g^2 + g'^2) + 2(3y_t^2 + 3y_b^2 + y_\tau^2)\lambda_5.
\end{aligned} \tag{A5}$$

The h_i's in type I are

$$\begin{aligned} &h_1^{\rm I}=h_3^{\rm I}=h_4^{\rm I}=h_5^{\rm I}=0,\\ &h_2^{\rm I}=4(3y_b^2+y_\tau^2)\lambda_2-4(3y_b^4+y_\tau^4). \end{aligned} \tag{A6}$$

The Yukawa couplings of the top quark, bottom quark, and tau lepton (y_t, y_b, and y_τ) are running with the β functions of

$$16\pi^2\beta_{y_f}^{\rm type}=c_{y_f}+h_{y_f}^{\rm type}, \qquad (f=t,b,\tau), \tag{A7}$$

where the common parts are

$$c_{y_t}=\left(-8g_s^2-\frac{9}{4}g^2-\frac{17}{12}g'^2+\frac{9}{2}y_t^2\right)y_t, \tag{A8}$$

$$\begin{aligned} &c_{y_b}=\left(-8g_s^2-\frac{9}{4}g^2-\frac{5}{12}g'^2+\frac{3}{2}y_t^2+\frac{9}{2}y_b^2\right)y_b,\\ &c_{y_\tau}=\left(-\frac{9}{4}g^2-\frac{15}{4}g'^2+\frac{5}{2}y_\tau^2\right)y_\tau, \end{aligned} \tag{A9}$$

and the type-dependent parts are

$$h_{y_t}^{\rm I}=\left(\frac{3}{2}y_b^2+y_\tau^2\right)y_t, \qquad h_{y_b}^{\rm I}=y_\tau^2 y_b, \qquad h_{y_\tau}^{\rm I}=3(y_t^2+y_b^2)y_\tau. \tag{A10}$$

The initial conditions of the Yukawa coupling are set at the top quark mass scale $m_t^{\rm pole}$ [26] as

$$\begin{aligned} &y_t(m_t^{\rm pole})=\frac{\sqrt{2}m_t}{vs_\beta}\left\{1-\frac{4}{3\pi}\alpha_s(m_t)\right\},\\ &y_b(m_t^{\rm pole})=\frac{\sqrt{2}m_b}{vs_\beta},\\ &y_\tau(m_t^{\rm pole})=\frac{\sqrt{2}m_\tau}{vs_\beta}. \end{aligned} \tag{A11}$$

---

[1] J. Ellis, SMEFT constraints on new physics beyond the standard model, in *The International Conference on Beyond Standard Model: From Theory to Experiment (BSM-2021)* (2021), 10.31526/ACP.BSM-2021.16.

[2] G. Aad *et al.* (ATLAS Collaboration), Measurements of WH and ZH production in the $H\to b\bar{b}$ decay channel in pp collisions at 13 TeV with the ATLAS detector, Eur. Phys. J. C **81**, 178 (2021).

[3] G. Aad *et al.* (ATLAS Collaboration), Measurements of Higgs bosons decaying to bottom quarks from vector boson fusion production with the ATLAS experiment at $\sqrt{s}=13$ TeV, Eur. Phys. J. C **81**, 537 (2021).

[4] A. M. Sirunyan *et al.* (CMS Collaboration), Inclusive search for highly boosted Higgs bosons decaying to bottom quark-antiquark pairs in proton-proton collisions at $\sqrt{s}=13$ TeV, J. High Energy Phys. 12 (2020) 085.

[5] ATLAS Collaboration, Study of Higgs-boson production with large transverse momentum using the $H\to b\bar{b}$ decay with the ATLAS detector, http://cds.cern.ch/record/2759284.

[6] A. Tumasyan *et al.* (CMS Collaboration), Measurement of the Inclusive and Differential Higgs Boson Production Cross Sections in the Decay Mode to a Pair of τ Leptons in pp Collisions at $\sqrt{s}=13$ TeV, Phys. Rev. Lett. **128**, 081805 (2022).

[7] ATLAS Collaboration, Measurement of the Higgs boson decaying to b-quarks produced in association with a top-quark pair in pp collisions at $\sqrt{s}=13$ TeV with the ATLAS detector, http://cds.cern.ch/record/2743685.

[8] ATLAS Collaboration, Measurements of gluon fusion and vector-boson-fusion production of the Higgs boson in $H\to WW^*\to e\nu\mu\nu$ decays using pp collisions at $\sqrt{s}=13$ TeV with the ATLAS detector, http://cds.cern.ch/record/2759651.

[9] ATLAS Collaboration, Measurement of the properties of Higgs boson production at $\sqrt{s}=13$ TeV in the $H\to\gamma\gamma$ channel using 139 fb^{-1} of pp collision data with the ATLAS experiment, http://cds.cern.ch/record/2725727.

[10] A. M. Sirunyan *et al.* (CMS Collaboration), Measurements of production cross sections of the Higgs boson in the four-lepton final state in proton–proton collisions at $\sqrt{s}=13$ TeV, Eur. Phys. J. C **81**, 488 (2021).

[11] G. Aad *et al.* (ATLAS Collaboration), Measurements of the Higgs boson inclusive and differential fiducial cross sections in the 4ℓ decay channel at $\sqrt{s}=13$ TeV, Eur. Phys. J. C **80**, 942 (2020).

[12] G. Aad *et al.* (ATLAS Collaboration), Higgs boson production cross-section measurements and their EFT interpretation in the 4ℓ decay channel at $\sqrt{s}=13$ TeV with the ATLAS detector, Eur. Phys. J. C **80**, 957 (2020).

[13] ATLAS Collaboration, A combination of measurements of Higgs boson production and decay using up to 139 fb^{-1} of proton–proton collision data at $\sqrt{s}=13$ TeV collected with the ATLAS experiment, http://cds.cern.ch/record/2725733.

[14] G. Aad *et al.* (ATLAS Collaboration), A search for the dimuon decay of the Standard Model Higgs boson with the ATLAS detector, Phys. Lett. B **812**, 135980 (2021).

[15] A. M. Sirunyan *et al.* (CMS Collaboration), Evidence for Higgs boson decay to a pair of muons, J. High Energy Phys. 01 (2021) 148.

[16] ATLAS Collaboration, Direct constraint on the Higgs-charm coupling from a search for Higgs boson decays to charm quarks with the ATLAS detector, http://cds.cern.ch/record/2771724.

[17] N. Turok and J. Zadrozny, Electroweak baryogenesis in the two doublet model, Nucl. Phys. **B358**, 471 (1991).

[18] A. G. Cohen, D. B. Kaplan, and A. E. Nelson, Spontaneous baryogenesis at the weak phase transition, Phys. Lett. B **263**, 86 (1991).

[19] V. Zarikas, The phase transition of the two Higgs extension of the standard model, Phys. Lett. B **384**, 180 (1996).

[20] J. M. Cline and P.-A. Lemieux, Electroweak phase transition in two Higgs doublet models, Phys. Rev. D **55**, 3873 (1997).

[21] L. Fromme, S. J. Huber, and M. Seniuch, Baryogenesis in the two-Higgs doublet model, J. High Energy Phys. 11 (2006) 038.

[22] M. E. Machacek and M. T. Vaughn, Two loop renormalization group equations in a general quantum field theory. 1. Wave function renormalization, Nucl. Phys. **B222**, 83 (1983).

[23] M. E. Machacek and M. T. Vaughn, Two loop renormalization group equations in a general quantum field theory. 2. Yukawa couplings, Nucl. Phys. **B236**, 221 (1984).

[24] M. E. Machacek and M. T. Vaughn, Two loop renormalization group equations in a general quantum field theory. 3. Scalar quartic couplings, Nucl. Phys. **B249**, 70 (1985).

[25] M.-x. Luo, H.-w. Wang, and Y. Xiao, Two loop renormalization group equations in general gauge field theories, Phys. Rev. D **67**, 065019 (2003).

[26] D. Das and I. Saha, Search for a stable alignment limit in two-Higgs-doublet models, Phys. Rev. D **91**, 095024 (2015).

[27] H. E. Haber and R. Hempfling, The renormalization group improved Higgs sector of the minimal supersymmetric model, Phys. Rev. D **48**, 4280 (1993).

[28] W. Grimus and L. Lavoura, Renormalization of the neutrino mass operators in the multi-Higgs-doublet standard model, Eur. Phys. J. C **39**, 219 (2005).

[29] D. Chowdhury and O. Eberhardt, Global fits of the two-loop renormalized two-Higgs-doublet model with soft Z_2 breaking, J. High Energy Phys. 11 (2015) 052.

[30] P. Basler, P. M. Ferreira, M. Mühlleitner, and R. Santos, High scale impact in alignment and decoupling in two-Higgs doublet models, Phys. Rev. D **97**, 095024 (2018).

[31] M. E. Krauss, T. Opferkuch, and F. Staub, The ultraviolet landscape of two-Higgs doublet models, Eur. Phys. J. C **78**, 1020 (2018).

[32] J. Oredsson and J. Rathsman, $\mathbb{Z}_2$ breaking effects in 2-loop RG evolution of 2HDM, J. High Energy Phys. 02 (2019) 152.

[33] M. Aiko and S. Kanemura, New scenario for aligned Higgs couplings originated from the twisted custodial symmetry at high energies, J. High Energy Phys. 02 (2021) 046.

[34] A. Dey, J. Lahiri, and B. Mukhopadhyaya, Muon $g-2$ and a type-X two-Higgs-doublet scenario: Some studies in high-scale validity, Phys. Rev. D **106**, 055023 (2022).

[35] S. Lee, K. Cheung, J. Kim, C.-T. Lu, and J. Song, Status of the two-Higgs-doublet model in light of the CDF mW measurement, Phys. Rev. D **106**, 075013 (2022).

[36] J. Kim, S. Lee, P. Sanyal, and J. Song, CDF W-boson mass and muon $g-2$ in a type-X two-Higgs-doublet model with a Higgs-phobic light pseudoscalar, Phys. Rev. D **106**, 035002 (2022).

[37] J. Kim, S. Lee, J. Song, and P. Sanyal, Fermiophobic light Higgs boson in the type-I two-Higgs-doublet model, Phys. Lett. B **834**, 137406 (2022).

[38] P. M. Ferreira, R. Santos, M. Sher, and J. P. Silva, Could the LHC two-photon signal correspond to the heavier scalar in two-Higgs-doublet models?, Phys. Rev. D **85**, 035020 (2012).

[39] S. Chang, S. K. Kang, J.-P. Lee, and J. Song, Higgs potential and hidden light Higgs scenario in two Higgs doublet models, Phys. Rev. D **92**, 075023 (2015).

[40] A. Jueid, J. Kim, S. Lee, and J. Song, Type-X two-Higgs-doublet model in light of the muon $g-2$: Confronting Higgs boson and collider data, Phys. Rev. D **104**, 095008 (2021).

[41] G. C. Branco, P. M. Ferreira, L. Lavoura, M. N. Rebelo, M. Sher, and J. P. Silva, Theory and phenomenology of two-Higgs-doublet models, Phys. Rep. **516**, 1 (2012).

[42] S. L. Glashow and S. Weinberg, Natural conservation laws for neutral currents, Phys. Rev. D **15**, 1958 (1977).

[43] E. A. Paschos, Diagonal neutral currents, Phys. Rev. D **15**, 1966 (1977).

[44] H. E. Haber and D. O'Neil, Basis-independent methods for the two-Higgs-doublet model. II. The significance of $\tan\beta$, Phys. Rev. D **74**, 015018 (2006).

[45] J. Song and Y. W. Yoon, $W\gamma$ decay of the elusive charged Higgs boson in the two-Higgs-doublet model with vector-like fermions, Phys. Rev. D **100**, 055006 (2019).

[46] S. Kanemura, Y. Okada, H. Taniguchi, and K. Tsumura, Indirect bounds on heavy scalar masses of the two-Higgs-doublet model in light of recent Higgs boson searches, Phys. Lett. B **704**, 303 (2011).

[47] J. Bernon, J. F. Gunion, H. E. Haber, Y. Jiang, and S. Kraml, Scrutinizing the alignment limit in two-Higgs-doublet models: $\mathrm{m}_h = 125$ GeV, Phys. Rev. D **92**, 075004 (2015).

[48] J. Bernon, J. F. Gunion, H. E. Haber, Y. Jiang, and S. Kraml, Scrutinizing the alignment limit in two-Higgs-doublet models. II. $\mathrm{m}_H = 125$ GeV, Phys. Rev. D **93**, 035027 (2016).

[49] T. Plehn, M. Spira, and P. M. Zerwas, Pair production of neutral Higgs particles in gluon-gluon collisions, Nucl. Phys. **B479**, 46 (1996).

[50] A. Djouadi, W. Kilian, M. Muhlleitner, and P. M. Zerwas, Production of neutral Higgs boson pairs at LHC, Eur. Phys. J. C **10**, 45 (1999).

[51] V. Barger, L. L. Everett, C. B. Jackson, and G. Shaughnessy, Higgs-pair production and measurement of the triscalar coupling at LHC(8,14), Phys. Lett. B **728**, 433 (2014).

[52] S. Dawson, A. Ismail, and I. Low, What's in the loop? The anatomy of double Higgs production, Phys. Rev. D **91**, 115008 (2015).

[53] K. Cheung, A. Jueid, C.-T. Lu, J. Song, and Y. W. Yoon, Disentangling new physics effects on nonresonant Higgs boson pair production from gluon fusion, Phys. Rev. D **103**, 015019 (2021).

[54] A. Jueid, J. Kim, S. Lee, and J. Song, Studies of nonresonant Higgs pair production at electron-proton colliders, Phys. Lett. B **819**, 136417 (2021).

[55] I. P. Ivanov, Minkowski space structure of the Higgs potential in 2HDM, Phys. Rev. D **75**, 035001 (2007).

[56] I. F. Ginzburg and I. P. Ivanov, Tree-level unitarity constraints in the most general 2HDM, Phys. Rev. D **72**, 115010 (2005).

[57] S. Kanemura and K. Yagyu, Unitarity bound in the most general two Higgs doublet model, Phys. Lett. B **751**, 289 (2015).

[58] A. Arhrib, Unitarity constraints on scalar parameters of the standard and two Higgs doublets model, in *Workshop on Noncommutative Geometry, Superstrings and Particle Physics* (2000), arXiv:hep-ph/0012353.

[59] I. P. Ivanov, General two-order-parameter Ginzburg-Landau model with quadratic and quartic interactions, Phys. Rev. E **79**, 021116 (2009).

[60] A. Barroso, P. M. Ferreira, I. P. Ivanov, R. Santos, and J. P. Silva, Evading death by vacuum, Eur. Phys. J. C **73**, 2537 (2013).

[61] A. Barroso, P. M. Ferreira, I. P. Ivanov, and R. Santos, Metastability bounds on the two Higgs doublet model, J. High Energy Phys. 06 (2013) 045.

[62] D. Eriksson, J. Rathsman, and O. Stal, 2HDMC: Two-Higgs-doublet model calculator physics and manual, Comput. Phys. Commun. **181**, 189 (2010).

[63] V. Branchina, F. Contino, and P. M. Ferreira, Electroweak vacuum lifetime in two Higgs doublet models, J. High Energy Phys. 11 (2018) 107.

[64] M. E. Peskin and T. Takeuchi, Estimation of oblique electroweak corrections, Phys. Rev. D **46**, 381 (1992).

[65] H.-J. He, N. Polonsky, and S.-f. Su, Extra families, Higgs spectrum and oblique corrections, Phys. Rev. D **64**, 053004 (2001).

[66] W. Grimus, L. Lavoura, O. M. Ogreid, and P. Osland, The oblique parameters in multi-Higgs-doublet models, Nucl. Phys. **B801**, 81 (2008).

[67] P. A. Zyla *et al.* (Particle Data Group), Review of particle physics, Prog. Theor. Exp. Phys. **2020**, 083C01 (2020).

[68] R. L. Workman *et al.* (Particle Data Group), Review of particle physics, Prog. Theor. Exp. Phys. **2022**, 083C01 (2022).

[69] A. Arbey, F. Mahmoudi, O. Stal, and T. Stefaniak, Status of the charged Higgs boson in two Higgs doublet models, Eur. Phys. J. C **78**, 182 (2018).

[70] P. Sanyal, Limits on the charged Higgs parameters in the two Higgs doublet model using CMS $\sqrt{s} = 13$ TeV results, Eur. Phys. J. C **79**, 913 (2019).

[71] M. Misiak and M. Steinhauser, Weak radiative decays of the B meson and bounds on $M_{H^\pm}$ in the two-Higgs-doublet model, Eur. Phys. J. C **77**, 201 (2017).

[72] P. Bechtle, S. Heinemeyer, T. Klingl, T. Stefaniak, G. Weiglein, and J. Wittbrodt, HiggsSignals-2: Probing new physics with precision Higgs measurements in the LHC 13 TeV era, Eur. Phys. J. C **81**, 145 (2021).

[73] M. Aaboud *et al.* (ATLAS Collaboration), Search for Higgs bosons produced via vector-boson fusion and decaying into bottom quark pairs in $\sqrt{s} = 13$ TeV pp collisions with the ATLAS detector, Phys. Rev. D **98**, 052003 (2018).

[74] M. Aaboud *et al.* (ATLAS Collaboration), Measurements of gluon-gluon fusion and vector-boson fusion Higgs boson production cross-sections in the $H \to WW^* \to e\nu\mu\nu$ decay channel in pp collisions at $\sqrt{s} = 13$ TeV with the ATLAS detector, Phys. Lett. B **789**, 508 (2019).

[75] M. Aaboud *et al.* (ATLAS Collaboration), Cross-section measurements of the Higgs boson decaying into a pair of τ-leptons in proton-proton collisions at $\sqrt{s} = 13$ TeV with the ATLAS detector, Phys. Rev. D **99**, 072001 (2019).

[76] G. Aad *et al.* (ATLAS Collaboration), Higgs boson production cross-section measurements and their EFT interpretation in the 4ℓ decay channel at $\sqrt{s} = 13$ TeV with the ATLAS detector, Eur. Phys. J. C **80**, 957 (2020).

[77] A. M. Sirunyan *et al.* (CMS Collaboration), Search for $\mathrm{t\bar{t}H}$ production in the $\mathrm{H} \to \mathrm{b\bar{b}}$ decay channel with leptonic $\mathrm{t\bar{t}}$ decays in proton-proton collisions at $\sqrt{s} = 13$ TeV, J. High Energy Phys. 03 (2019) 026.

[78] A. M. Sirunyan *et al.* (CMS Collaboration), Search for the Higgs Boson Decaying to Two Muons in Proton-Proton Collisions at $\sqrt{s} = 13$ TeV, Phys. Rev. Lett. **122**, 021801 (2019).

[79] CMS Collaboration, Measurements of properties of the Higgs boson in the four-lepton final state in proton-proton collisions at $\sqrt{s} = 13$ TeV, http://cds.cern.ch/record/2668684.

[80] CMS Collaboration, Measurements of differential Higgs boson production cross sections in the leptonic WW decay mode at $\sqrt{s} = 13$ TeV, http://cds.cern.ch/record/2691268.

[81] P. Bechtle, D. Dercks, S. Heinemeyer, T. Klingl, T. Stefaniak, G. Weiglein, and J. Wittbrodt, HiggsBounds-5: Testing Higgs sectors in the LHC 13 TeV era, Eur. Phys. J. C **80**, 1211 (2020).

[82] T. Aaltonen *et al.* (CDF Collaboration), High-precision measurement of the W boson mass with the CDF II detector, Science **376**, 170 (2022).

[83] C.-T. Lu, L. Wu, Y. Wu, and B. Zhu, Electroweak precision fit and new physics in light of the W boson mass, Phys. Rev. D **106**, 035034 (2022).

[84] Y.-Z. Fan, T.-P. Tang, Y.-L. S. Tsai, and L. Wu, Inert Higgs Dark Matter for CDF II W-Boson Mass and Detection Prospects, Phys. Rev. Lett. **129**, 091802 (2022).

[85] C.-R. Zhu, M.-Y. Cui, Z.-Q. Xia, Z.-H. Yu, X. Huang, Q. Yuan *et al.*, Explaining the GeV antiproton/$\gamma-$ray excesses and W-boson mass anomaly in an inert two Higgs doublet model, arXiv:2204.03767.

[86] B.-Y. Zhu, S. Li, J.-G. Cheng, R.-L. Li, and Y.-F. Liang, Using gamma-ray observation of dwarf spheroidal galaxy

to test a dark matter model that can interpret the W-boson mass anomaly, arXiv:2204.04688.
[87] H. Song, W. Su, and M. Zhang, Electroweak phase transition in 2HDM under Higgs, Z-pole, and W precision measurements, J. High Energy Phys. 10 (2022) 048.
[88] H. Bahl, J. Braathen, and G. Weiglein, New physics effects on the W-boson mass from a doublet extension of the SM Higgs sector, Phys. Lett. B **833**, 137295 (2022).
[89] Y. Heo, D.-W. Jung, and J. S. Lee, Impact of the CDF W-mass anomaly on two Higgs doublet model, Phys. Lett. B **833**, 137274 (2022).
[90] K. S. Babu, S. Jana, and P. K. Vishnu, Correlating W-Boson Mass Shift with Muon $g-2$ in the Two Higgs Doublet Model, Phys. Rev. Lett. **129**, 121803 (2022).
[91] T. Biekötter, S. Heinemeyer, and G. Weiglein, Excesses in the low-mass Higgs-boson search and the W-boson mass measurement, arXiv:2204.05975.
[92] Y. H. Ahn, S. K. Kang, and R. Ramos, Implications of new CDF-II W boson mass on two Higgs doublet model, Phys. Rev. D **106**, 055038 (2022).
[93] X.-F. Han, F. Wang, L. Wang, J. M. Yang, and Y. Zhang, Joint explanation of W-mass and muon $g-2$ in the 2HDM*, Chin. Phys. C **46**, 103105 (2022).
[94] G. Arcadi and A. Djouadi, 2HD plus light pseudoscalar model for a combined explanation of the possible excesses in the CDF MW measurement and $(g-2)\mu$ with dark matter, Phys. Rev. D **106**, 095008 (2022).
[95] K. Ghorbani and P. Ghorbani, W-boson mass anomaly from scale invariant 2HDM, Nucl. Phys. **B984**, 115980 (2022).
[96] A. Broggio, E. J. Chun, M. Passera, K. M. Patel, and S. K. Vempati, Limiting two-Higgs-doublet models, J. High Energy Phys. 11 (2014) 058.
[97] J. Oredsson, 2HDME: Two-Higgs-doublet model evolver, Comput. Phys. Commun. **244**, 409 (2019).
[98] I. P. Ivanov, Minkowski space structure of the Higgs potential in 2HDM. II. Minima, symmetries, and topology, Phys. Rev. D **77**, 015017 (2008).
[99] A. G. Akeroyd, Fermiophobic Higgs bosons at the Tevatron, Phys. Lett. B **368**, 89 (1996).
[100] A. G. Akeroyd, Fermiophobic and other nonminimal neutral Higgs bosons at the LHC, J. Phys. G **24**, 1983 (1998).
[101] A. Barroso, L. Brucher, and R. Santos, Is there a light fermiophobic Higgs?, Phys. Rev. D **60**, 035005 (1999).
[102] L. Brucher and R. Santos, Experimental signatures of fermiophobic Higgs bosons, Eur. Phys. J. C **12**, 87 (2000).
[103] A. G. Akeroyd, M. A. Diaz, and F. J. Pacheco, Double fermiophobic Higgs boson production at the CERN LHC and LC, Phys. Rev. D **70**, 075002 (2004).
[104] A. Arhrib, R. Benbrik, R. B. Guedes, and R. Santos, Search for a light fermiophobic Higgs boson produced via gluon fusion at Hadron Colliders, Phys. Rev. D **78**, 075002 (2008).
[105] E. L. Berger, Z. Sullivan, and H. Zhang, Associated Higgs plus vector boson test of a fermiophobic Higgs boson, Phys. Rev. D **86**, 015011 (2012).
[106] V. Ilisie and A. Pich, Low-mass fermiophobic charged Higgs phenomenology in two-Higgs-doublet models, J. High Energy Phys. 09 (2014) 089.
[107] A. Delgado, M. Garcia-Pepin, M. Quiros, J. Santiago, and R. Vega-Morales, Diphoton and diboson probes of fermiophobic Higgs bosons at the LHC, J. High Energy Phys. 06 (2016) 042.
[108] T. Mondal and P. Sanyal, Same sign trilepton as signature of charged Higgs in two Higgs doublet model, J. High Energy Phys. 05 (2022) 040.
[109] K. Cheung, A. Jueid, J. Kim, S. Lee, C.-T. Lu, and J. Song, Comprehensive study of the light charged Higgs boson in the type-I two-Higgs-doublet model, Phys. Rev. D **105**, 095044 (2022).
[110] M. Forslund and P. Meade, High precision Higgs from high energy muon colliders, J. High Energy Phys. 08 (2022) 185.
[111] M. Misiak, A. Rehman, and M. Steinhauser, Towards $\bar{B} \to X_s\gamma$ at the NNLO in QCD without interpolation in m_c, J. High Energy Phys. 06 (2020) 175.
[112] A. Djouadi, The anatomy of electro-weak symmetry breaking. II. The Higgs bosons in the minimal supersymmetric model, Phys. Rep. **459**, 1 (2008).
[113] C. Degrande, C. Duhr, B. Fuks, D. Grellscheid, O. Mattelaer, and T. Reiter, UFO—The universal FeynRules output, Comput. Phys. Commun. **183**, 1201 (2012).
[114] A. Alloul, N. D. Christensen, C. Degrande, C. Duhr, and B. Fuks, FeynRules 2.0—A complete toolbox for tree-level phenomenology, Comput. Phys. Commun. **185**, 2250 (2014).
[115] J. Alwall, M. Herquet, F. Maltoni, O. Mattelaer, and T. Stelzer, MadGraph 5: Going beyond, J. High Energy Phys. 06 (2011) 128.
[116] R. D. Ball *et al.* (NNPDF Collaboration), Parton distributions from high-precision collider data, Eur. Phys. J. C **77**, 663 (2017).
[117] J. Baglio, A. Djouadi, R. Gröber, M. M. Mühlleitner, J. Quevillon, and M. Spira, The measurement of the Higgs self-coupling at the LHC: Theoretical status, J. High Energy Phys. 04 (2013) 151.
[118] ATLAS Collaboration, Measurement prospects of the pair production and self-coupling of the Higgs boson with the ATLAS experiment at the HL-LHC, http://cds.cern.ch/record/2652727.
[119] A. Ballestrero, G. Bevilacqua, and E. Maina, A complete parton level analysis of boson-boson scattering and electroweak symmetry breaking in lv + four jets production at the LHC, J. High Energy Phys. 05 (2009) 015.
[120] S. Jung, Z. Liu, L.-T. Wang, and K.-P. Xie, Probing Higgs boson exotic decays at the LHC with machine learning, Phys. Rev. D **105**, 035008 (2022).
[121] M. Bicer *et al.* (TLEP Design Study Working Group), First look at the physics case of TLEP, J. High Energy Phys. 01 (2014) 164.
[122] J. Gao, CEPC and SppC status—from the completion of CDR towards TDR, Int. J. Mod. Phys. A **36**, 2142005 (2021).

[123] M. Dong *et al.* (CEPC Study Group), CEPC conceptual design report: Volume 2—physics & detector, arXiv:1811.10545.

[124] R. B. Palmer, J. S. Berg, R. C. Fernow, J. C. Gallardo, H. G. Kirk, Y. Alexahin *et al.*, A complete scheme of ionization cooling for a muon collider, Conf. Proc. C **070625**, 3193 (2007).

[125] J. P. Delahaye, M. Diemoz, K. Long, B. Mansoulié, N. Pastrone, L. Rivkin *et al.*, Muon colliders, arXiv:1901.06150.

[126] K. M. Black *et al.*, Muon collider forum report, arXiv:2209.01318.

[127] T. P. Cheng, E. Eichten, and L.-F. Li, Higgs phenomena in asymptotically free gauge theories, Phys. Rev. D **9**, 2259 (1974).

[128] H. Komatsu, Behavior of the Yukawa and the quartic scalar couplings in grand unified theories, Prog. Theor. Phys. **67**, 1177 (1982).